

The Shape of a Möbius Strip via Elastic Rod Theory Revisited

Alexander Moore · Timothy J. Healey

May 15, 2022

Abstract In 1993 Mahadevan and Keller used the Kirchhoff rod theory to predict the shape of a Möbius band. Starting from the solution for a square cross-section (isotropic), they employ numerical continuation in the cross-sectional aspect ratio in order to approach the solution for a thin strip. Certain smoothly varying configurations are obtained. More recently in 2007, Starostin and van der Heijden pointed out that an actual Möbius band “localizes” into a nearly flat triangular configuration as the ratio of the strip width to center-line circumference is no longer small. Accordingly they return to the developable, thin-plate model of Sadowsky and Wunderlich, obtaining such localized shapes. In this work we strike a middle ground between these two approaches. We employ the standard two-director (special) Cosserat model, and we also use the cross-sectional aspect ratio as a numerical continuation parameter. Nonetheless, we are able to capture both the smoothly varying shapes and the localized, nearly triangular configurations. Our point of departure is that we do not always employ the strength-of-materials formula for the torsional stiffness - a standard feature of the Kirchhoff theory. Our key observation comes from the usual Cosserat ansatz in light of developability, suggesting an increasing torsional stiffness ratio (as well as one increasing bending stiffness ratio) as the thickness becomes small. We demonstrate that the closed-loop configurations we obtain are stable with respect to small perturbations.

Keywords Cosserat rod theory · Developable surface · Stability

Mathematics Subject Classification (2000) 74K10 · 34B60

1 Introduction

Sadowsky [14] was apparently the first to model a Möbius band as a thin elastic structure in order to predict its shape. Formed by twisting one end of a long, flat, rectangular strip

A. Moore
Field of Theoretical and Applied Mechanics, Cornell University, Ithaca, NY, USA
E-mail: amm456@cornell.edu

T. J. Healey
Department of Mathematics, Cornell University, Ithaca, NY, USA
E-mail: tjh10@cornell.edu

of, say, paper by 180 degrees and then gluing it smoothly to the other end, the band is the quintessential example of a non-orientable 2-surface. The main idea in [14], also followed upon later by Wunderlich [18], is the idealization of the strip as a thin elastic plate with its mid-plane deforming isometrically, i.e., the deformed mid-surface is developable. Aspects of the resulting potential energy functional are addressed in [14, 18] without solving for the specific shape of the band.

In 1993 Mahadevan and Keller [13] considered the shape problem, modeling the strip as a classical Kirchhoff rod. In particular, the ratio of the two bending moduli (equal to the square of the aspect ratio of the cross-section) is used as a numerical continuation parameter. The procedure cleverly initiates from the isotropic case (aspect ratio of 1), for which the problem admits a closed-form solution. As the parameter becomes very large, one bending direction becomes a great deal stiffer than the other, and the solutions purportedly approach that of a thin strip. In this way, certain smoothly varying configurations are obtained in good agreement with the shape of some Möbius bands as depicted in [13].

More recently Starostin and van der Heijden [16] returned to the same question, noting that a Möbius band localizes into three, nearly flat triangular regions when the width of the strip is not small compared to its circumference. As pointed out in [16], such behavior cannot be captured by the standard Kirchhoff rod model, as verified by the exclusively smooth configurations found in [13]. Accordingly they return to the developable-surface plate model of [14] and [18]. Such a surface is necessarily ruled, and stationary potential energy yields generalized (Cosserat) rod equilibrium equations. The latter correspond to the standard rod equilibrium equations (local balance of forces and moments) with constraints, augmented by an extra “internal variable and a concomitant balance law, cf. also [3, 11, 17]. The equilibrium equations are subsequently solved apparently by numerical continuation using the width-to-circumference ratio as the parameter. We remark that it is unclear how this continuation initiates, given that no closed-form solution exists. In any case, the above-mentioned localized solutions are found and presented in [16].

We strike a middle ground between these two approaches. As in [13], we use the standard 2-director (special) Cosserat rod theory, and we also employ the square of the cross-sectional aspect ratio as an increasing continuation parameter. Nonetheless, we are able to capture localized shapes, as discussed in [16], as well as the smoothly varying configurations of [13]. Our point of departure is the following: In contrast to [13], we do not rely upon the strength-of-materials formula for the torsional stiffness - a particular feature of the Kirchhoff theory. Our key observation comes from viewing the special Cosserat ansatz in light of developability (of the mid-surface). In particular, this suggests an ever-increasing torsional stiffness in order to approach a developable mid-surface.

The outline of the paper is as follows: In Section 2 we formulate the problem as a hyperelastic, inextensible, unsharable rod characterized by a quadratic, positive-definite, uncoupled stored energy function in the two bending curvatures and the twist. We call the model a *Kirchhoff rod* in the case when all three elastic moduli are determined by the usual strength-of-materials formulas. Otherwise, we refer to the model as a *Cosserat rod*. In particular, the justification for an increasing torsional modulus in light of developability is given in this section. The resulting model is called a Cosserat rod.

We discuss the numerical implementation of the problem in Section 3. As in [8] and [13], we analyze only half of the rod with appropriate boundary conditions enabling the generation of a complete solution of the band via a 180 degree flip symmetry. Continuation initiates from the isotropic case. Following the methodology in [10], we employ quaternions (in lieu of Euler angles). For a general class of rod problems, this formulation ensures a

consistent count of boundary conditions and unknowns, as well as the numerical accuracy of both the solution and the point-wise unit magnitude of the quaternion field.

In Section 4 we present the results for both the Kirchhoff rod and the Cosserat rod. The former is characterized by a fixed relative torsional stiffness, and we obtain solutions akin to those found in [13]. On the other hand, the Cosserat model features a torsional-modulus ratio that, like the bending-modulus ratio, grows linearly in the continuation parameter. Interestingly we obtain the localized behavior, as discussed in [16], only when the linear growth rate for the torsional-stiffness ratio is slightly larger than that of the bending-stiffness ratio. In Section 5 we use the approach of [12], based on linearized dynamics, to deduce the local stability of the entire closed configuration. To the best of our knowledge, these are the first stability results for the equilibrium solutions of a Möbius band.

2 Formulation

Let $\{\mathbf{e}_1, \mathbf{e}_2, \mathbf{e}_3\}$ denote a fixed, right-handed, orthonormal basis for \mathbf{E}^3 , the translate space for 3-dimensional Euclidean point space. We start by defining the special Cosserat rod with centerline coordinate $s \in [0, 1]$ in a straight, stress-free reference configuration. The position of the rod is defined by the vector-valued function $\mathbf{r} : [0, 1] \rightarrow \mathbb{R}^3$ with the reference configuration's centerline given by $\mathbf{r}(s) = s\mathbf{e}_3$. The cross-sections of the rod in the reference configuration are parallel to the plane span $\{\mathbf{e}_1, \mathbf{e}_2\}$. Let $\mathbf{R}(s)$ denote the rotation of the cross-sectional plane parallel to span $\{\mathbf{e}_1, \mathbf{e}_2\}$ at s in the undeformed rod.

We define the orthonormal basis field $\{\mathbf{d}_1, \mathbf{d}_2, \mathbf{d}_3\}$ via

$$\mathbf{d}_i(s) = \mathbf{R}(s) \mathbf{e}_i. \quad (1)$$

The configuration of the rod is uniquely determined by the functions $\mathbf{r}(s)$ and $\mathbf{R}(s)$. Differentiation of (1) yields

$$\mathbf{d}'_i = \mathbf{R}' \mathbf{e}_i = \mathbf{R}' \mathbf{R}^T \mathbf{d}_i = \mathbf{K} \mathbf{d}_i, \quad (2)$$

where $\mathbf{K} \equiv \mathbf{R}' \mathbf{R}^T$ is a skew-symmetric tensor field. Thus, there is a unique vector field, $\boldsymbol{\kappa}$, the axial vector field of \mathbf{K} , such that

$$\mathbf{d}'_i = \boldsymbol{\kappa} \times \mathbf{d}_i, \quad (3)$$

where $\mathbf{a} \times \mathbf{b}$ denotes the usual right-handed cross product for $\mathbf{a}, \mathbf{b} \in \mathbf{E}^3$. We define the strain variables $\mathbf{v}, \boldsymbol{\kappa}$ via

$$\mathbf{r}' = v_i \mathbf{d}_i, \quad (4)$$

$$\boldsymbol{\kappa} = \kappa_i \mathbf{d}_i, \quad (5)$$

where here and throughout we employ the summation convention with Latin indices are summed over components 1 to 3, and Greek indices are summed over components 1 to 2. The component fields v_i and κ_i , $i = 1, 2, 3$, are the strains of the theory: v_1, v_2 correspond to “shear” strains, v_3 the “extension”, κ_1, κ_2 are “curvatures” of the rod, and κ_3 is the “twist” of the rod. In particular, $0 < v_3 < \infty$, while other strains can take on any real value.

Henceforth, we assume that the rod is *unshearable* and *inextensible*, corresponding to the constraint

$$\mathbf{r}' \equiv \mathbf{d}_3. \quad (6)$$

The vector fields $\mathbf{n}(s)$ and $\mathbf{m}(s)$, denote the internal contact force and contact couple, respectively, acting on the deformed cross section. We write

$$\mathbf{n} = n_i \mathbf{d}_i, \quad (7)$$

$$\mathbf{m} = m_i \mathbf{d}_i, \quad (8)$$

where the component fields, n_i and m_i , $i = 1, 2, 3$, are the internal forces and moments respectively: n_1, n_2 correspond to “shear forces”; n_3 “axial” force; m_1, m_2 correspond to bending moments, and m_3 to torque or twisting moment. In the absence of body forces and body couples, the local form of force and moment balance are given by

$$\mathbf{n}' = 0, \quad (9)$$

$$\mathbf{m}' + \mathbf{d}_3 \times \mathbf{n} = 0, \quad (10)$$

respectively where we have used (6). In this formulation, the contact force \mathbf{n} is Lagrange multiplier enforcing the unshearable-inextensible constraint (6).

We define an *objective, hyperelastic, inextensible and unshearable rod* as one characterized by the existence of a non-negative C^2 function $W : \mathbb{R}^3 \rightarrow [0, \infty)$, called the *stored energy density*, such that

$$m_i = \frac{\partial W}{\partial \kappa_i}, \quad i = 1, 2, 3. \quad (11)$$

For notational convenience, we denote the following triples of real number via

$$\mathbf{k} := (\kappa_1, \kappa_2, \kappa_3) \quad \mathbf{v} := (v_1, v_2, v_3) \quad \mathbf{n} := (n_1, n_2, n_3) \quad \mathbf{m} := (m_1, m_2, m_3) \quad (12)$$

Writing $W(\mathbf{k}) \equiv W(\kappa_1, \kappa_2, \kappa_3)$, then (11) takes the compact form

$$\mathbf{m} = \frac{dW}{d\mathbf{k}}. \quad (13)$$

Rewriting the balance of forces and balance of moments equations (9)-(10) relative to the director field $\{\mathbf{d}_1, \mathbf{d}_2, \mathbf{d}_3\}$ gives

$$\mathbf{n}' + \mathbf{k} \times \mathbf{n} = 0, \quad (14)$$

$$\mathbf{m}' + \mathbf{k} \times \mathbf{m} + \hat{\mathbf{d}} \times \mathbf{n} = 0, \quad (15)$$

with $\hat{\mathbf{d}} := (0, 0, 1)$. The kinematic equations for the rod position and orientation (\mathbf{r}, \mathbf{R}) with respect to the fixed $\{\mathbf{e}_1, \mathbf{e}_2, \mathbf{e}_3\}$ basis are expressed by

$$\bar{\mathbf{r}}' = \bar{\mathbf{R}} \hat{\mathbf{d}}, \quad (16)$$

$$\bar{\mathbf{R}}' = \bar{\mathbf{R}} \mathbf{K}, \quad (17)$$

where \mathbf{K} is the unique skew symmetric matrix satisfying $\mathbf{k} = \text{axial}(\mathbf{K})$ and $\bar{\mathbf{R}}$ is the matrix of \mathbf{R} relative to the fixed basis $\{\mathbf{e}_1, \mathbf{e}_2, \mathbf{e}_3\}$. Henceforth, all components written with respect to the fixed $\{\mathbf{e}_i\}$ basis are denoted by an over-bar, e.g. $\mathbf{r}' = \bar{r}'_i \mathbf{e}_i$, $\bar{\mathbf{r}} = (\bar{r}_1, \bar{r}_2, \bar{r}_3)$, while quantities expressed with respect to the convected $\{\mathbf{d}_i\}$ basis are written in san-serif font as in (12).

We assume the simplest quadratic form for the stored energy density, viz.,

$$W(\mathbf{k}) = \frac{1}{2} \alpha_i \kappa_i^2, \quad (18)$$

where the $\alpha_i > 0$, $i = 1, 2, 3$ are the elastic moduli. In the classical *Kirchhoff model*, for example, we have the strength-of-materials type formulas for the elastic moduli:

$$\alpha_\ell = EI_\ell, \quad \ell = 1, 2 \quad (19)$$

$$\alpha_3 = GJ, \quad (20)$$

where E denotes the Young's modulus of elasticity, G denotes the shear modulus, I_ℓ is the area moment of inertia, $\ell = 1, 2$, and J denotes the (weighted) polar area moment of inertia [2]. Here, we assume the normalization: $\alpha_1 = 1$, $\alpha_2 = \lambda$, $\alpha_3 = \gamma$, and thus from (13) we have

$$m_1 = \kappa_1, \quad (21)$$

$$m_2 = \lambda \kappa_2, \quad (22)$$

$$m_3 = \gamma \kappa_3. \quad (23)$$

In view of (19), we may think of λ as the ratio of the two area moments of inertia of the cross section, which we take to be very large for *thin* rectangular cross sections, viz., its thickness is much smaller than its other dimension. As pointed out in [16], if the torsional modulus is interpreted in the same manner, viz., according to (20) giving $\gamma = GJ/EI_1$, the model does not capture the correct localized behavior of a thin rectangular strip forming a Möbius band.

In order to motivate our model, we consider the usual ansatz for a (special) Cosserat rod modeled as a constrained 3-dimensional body [1]:

$$\mathbf{x} = \mathbf{r}(s) + X_\alpha \mathbf{d}_\alpha(s), \quad (24)$$

where (X_1, X_2, s) denotes the Cartesian coordinates of the material point in the reference configuration, while \mathbf{x} denotes the position of the same material point in the deformed configuration. We take X_2 as the coordinate in the small-thickness direction and consider (24) at the mid-surface $X_2 = 0$:

$$\mathbf{x}_0 := \mathbf{r}(s) + X_1 \mathbf{d}_1(s). \quad (25)$$

If this *constrained* mid-surface is *developable*, then we must have (cf. [4])

$$\mathbf{r}' \cdot (\mathbf{d}_1 \times \mathbf{d}_1') = 0. \quad (26)$$

Using (3) and (6) in (26), we find that

$$\kappa_3 \equiv 0. \quad (27)$$

Moreover, from (3), (6), and (25) we obtain the matrix of the first fundamental form:

$$\begin{bmatrix} 1 & 0 \\ 0 & 1 + (X_1)^2 |\boldsymbol{\kappa} \times \mathbf{d}_1|^2 \end{bmatrix}, \quad (28)$$

which in this case coincides with the matrix of the right Cauchy-Green strain tensor with respect to the fixed basis $\{\mathbf{e}_1, \mathbf{e}_3\}$. We conclude that (25) defines an isometry if and only if $\boldsymbol{\kappa}$ is parallel to \mathbf{d}_1 , i.e. in addition to (27), we have

$$\kappa_2 \equiv 0. \quad (29)$$

We do not strictly enforce (27) and (29). Indeed, (24) per se is only approximate. Nonetheless (29) motivates taking λ very large in (21)-(22) as done in [13], while (27) further motivates, say,

$$\gamma = f(\lambda), \quad f: \mathbb{R}^+ \rightarrow \mathbb{R}^+, \quad (30)$$

such that $f \rightarrow \infty$ as $\lambda \rightarrow \infty$. For simplicity, we choose here

$$\gamma = c\lambda, \quad (31)$$

yielding

$$m_3 = c\lambda \kappa_3. \quad (32)$$

with c a positive constant.

3 Solution Method

Following the approach in [8], [13] and [16], we search for closed loop solutions of (14)-(17) that possess a *flip symmetry* about, say, the \mathbf{e}_2 axis. That is, we suppose that a rotation by 180 degrees of the closed rod about the \mathbf{e}_2 axis is a symmetry of the configuration. Hence we solve (14)-(17) for half of the rod with appropriate boundary conditions, and generate the full loop solution by symmetry.

We solve the resulting two-point boundary value problem with numerical continuation via the software package AUTO [6]. As in [13], we start the continuation from the equilibrium configuration of a twisted rod with equal bending stiffnesses, and then follow the path of equilibria as the constitutive parameter λ increases.

3.1 Numerical Parameterization

As in [10] we parameterize \bar{R} in (16) via quaternions, thus avoiding the usual singularities, associated with Euler angles. Accordingly (16)-(17) are replaced by

$$\bar{r}' = \bar{R}(\mathbf{q}) \hat{\mathbf{d}}, \quad (33)$$

$$\mathbf{q}' = \bar{A}(\mathbf{q}) \mathbf{k}, \quad (34)$$

respectively, with $\mathbf{q} := (q_0, q_1, q_2, q_3)$ subject to the normalization

$$q_0^2 + q_1^2 + q_2^2 + q_3^2 = 1. \quad (35)$$

The formulas for $\bar{R}(\mathbf{q})$ and $\bar{A}(\mathbf{q})$ are as follows (cf. [10]):

$$\bar{R}(\mathbf{q}) = 2 \begin{pmatrix} q_0^2 + q_1^2 - 1/2 & q_1 q_2 - q_0 q_3 & q_1 q_3 + q_0 q_2 \\ q_1 q_2 + q_0 q_3 & q_0^2 + q_2^2 - 1/2 & q_2 q_3 - q_0 q_1 \\ q_1 q_3 - q_0 q_2 & q_2 q_3 + q_0 q_1 & q_0^2 + q_3^2 - 1/2 \end{pmatrix}, \quad (36)$$

$$\bar{A}(\mathbf{q}) = \frac{1}{2} \begin{pmatrix} -q_1 & -q_2 & -q_3 \\ q_0 & -q_3 & q_2 \\ q_3 & q_0 & -q_1 \\ -q_2 & q_1 & q_0 \end{pmatrix}. \quad (37)$$

In general, an accurate solution of (33)-(34) (satisfying reasonable boundary conditions) need not satisfy (35) with accuracy. We follow the approach in [10] and replace (34) with the augmented equation containing a multiplier $\mu \in \mathbb{R}$:

$$\mathbf{q}' = \bar{A}(\mathbf{q}) \mathbf{k} + \mu \mathbf{q} \quad (38)$$

Use of (38) ensures that (35) will be satisfied identically along the entire length of the rod whenever (35) is merely enforced on the boundary points. In practice, it turns out that the multiplier μ takes on numerical values close to zero (typically $\mu = O(10^{-8})$), c.f. [10].

Combining (14), (15), (21)-(23), (33), and (38) we arrive at the full governing system:

$$\mathbf{n}' + \tilde{\mathbf{k}}(\mathbf{m}) \times \mathbf{n} = 0, \quad (39)$$

$$\mathbf{m}' + \tilde{\mathbf{k}}(\mathbf{m}) \times \mathbf{m} + \hat{\mathbf{d}} \times \mathbf{n} = 0, \quad (40)$$

$$\bar{\mathbf{r}}' - \bar{\mathbf{R}}(\mathbf{q}) \hat{\mathbf{d}} = 0, \quad (41)$$

$$\mathbf{q}' - \bar{A}(\mathbf{q}) \tilde{\mathbf{k}}(\mathbf{m}) - \mu \mathbf{q} = 0. \quad (42)$$

where

$$\tilde{\mathbf{k}}(\mathbf{m}) := \left(m_1, \frac{m_2}{\lambda}, \frac{m_3}{\gamma} \right). \quad (43)$$

3.2 Boundary Conditions

Equations (39)-(42) constitute a system of first order ODE's in 14 unknowns $(\bar{\mathbf{r}}, \mathbf{n}, \mathbf{m}, \mathbf{q}, \mu)$ and the material parameter λ . Thus the problem requires 14 boundary conditions. We consider a half-rod of length π (so that the Möbius strip has total length 2π). The position and orientation of the rod at $s = 0$ are fixed at a particular point in \mathbb{R}^3 , yielding

$$\mathbf{r}(0) \cdot \mathbf{e}_1 = \bar{r}_1(0) = 0, \quad (44)$$

$$\mathbf{r}(0) \cdot \mathbf{e}_2 = \bar{r}_2(0) = 1, \quad (45)$$

$$\mathbf{r}(0) \cdot \mathbf{e}_3 = \bar{r}_3(0) = 0, \quad (46)$$

$$\mathbf{q}(0) = (q_0, q_1, q_2, q_3) = (1, 0, 0, 0). \quad (47)$$

This gives seven boundary conditions. We note that (47) fulfills (35), specifying

$$\bar{\mathbf{R}}(\mathbf{q}(0)) = \bar{\mathbf{I}}, \quad (48)$$

where $\bar{\mathbf{I}}$ is the 3×3 identity matrix.

For the boundary conditions at $s = \pi$, we place a perfect hinge parallel to \mathbf{e}_2 , along which the rod may freely slide and about which freely rotate. From this, the boundary conditions at $s = \pi$ become

$$\mathbf{r}(\pi) \cdot \mathbf{e}_1 = \bar{r}_1(\pi) = 0, \quad (49)$$

$$\mathbf{r}(\pi) \cdot \mathbf{e}_3 = \bar{r}_3(\pi) = 0, \quad (50)$$

$$\mathbf{n}(\pi) \cdot \mathbf{e}_2 = n_1(\pi) = 0, \quad (51)$$

$$\mathbf{m}(\pi) \cdot \mathbf{e}_2 = m_1(\pi) = 0. \quad (52)$$

In addition, the rod will twist by a quarter turn from the orientation in (48). Accordingly we choose the directors at $s = \pi$ as follows:

$$\mathbf{d}_1(\pi) = -\mathbf{e}_2, \quad (53)$$

$$\mathbf{d}_2(\pi) = \cos \beta \mathbf{e}_1 + \sin \beta \mathbf{e}_3, \quad (54)$$

$$\mathbf{d}_3(\pi) = -\sin \beta \mathbf{e}_1 + \cos \beta \mathbf{e}_3. \quad (55)$$

where β is some unspecified angle. In particular, (53) justifies the subscript “1” in (51) and (52). From (53)-(55), we know that the rotation matrix at $s = \pi$ is given by

$$\bar{\mathbf{R}}(\mathbf{q}(\pi)) = \begin{bmatrix} 0 & \cos \beta & -\sin \beta \\ -1 & 0 & 0 \\ 0 & \sin \beta & \cos \beta \end{bmatrix}. \quad (56)$$

Comparing (56) to (36), we may choose the two boundary conditions,

$$q_0^2(\pi) + q_2^2(\pi) - \frac{1}{2} = 0, \quad (57)$$

$$q_2(\pi) q_3(\pi) - q_0(\pi) q_1(\pi) = 0, \quad (58)$$

and add the normalization

$$q_1^2(\pi) + q_2^2(\pi) + q_3^2(\pi) + q_0^2(\pi) = 1. \quad (59)$$

This completes the required set of 14 boundary conditions.

3.3 Starting Equilibrium Configuration

The starting equilibrium configuration is a rod with equal bending moduli in a semi-circular configuration which is rotated clockwise (from the viewpoint of $s = 0$) by a total angle of $\pi/2$ at $s = \pi$, c.f. Figure 1. The configuration for the half-rod defines the configuration of the full Möbius strip on $s \in [0, 2\pi]$ via reflection about the \mathbf{e}_2 axis.

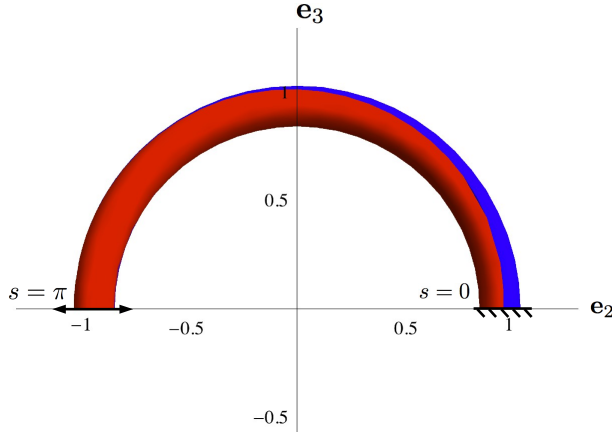


Fig. 1 The rod in its starting configuration with a fixed end at $s = 0$ and a hinged end free to slide along the \mathbf{e}_2 axis at $s = \pi$. The coloring is presented to show orientation of the material points of the rod as the cross-sections rotate clockwise about \mathbf{d}_3 from $s = 0$ to $s = \pi$.

The explicit starting equilibrium configuration is:

$$\begin{array}{ll} \text{Parameters:} & \lambda = 1 \\ & \gamma = (\text{to be determined later}) \\ & \mu = 0 \end{array} \quad (60)$$

$$\begin{array}{ll} \text{Positions:} & \bar{\mathbf{r}}_1 = \mathbf{0} \\ & \bar{\mathbf{r}}_2 = \cos(s) \\ & \bar{\mathbf{r}}_3 = \sin(s) \end{array} \quad (61)$$

$$\begin{array}{ll} \text{Forces:} & \mathbf{n}_1 = \frac{1}{2} \gamma \cos\left(\frac{1}{2}s\right) \\ & \mathbf{n}_2 = -\frac{1}{2} \gamma \sin\left(\frac{1}{2}s\right) \\ & \mathbf{n}_3 = 0 \end{array} \quad (62)$$

$$\begin{array}{ll} \text{Moments:} & \mathbf{m}_1 = \cos\left(\frac{1}{2}s\right) \\ & \mathbf{m}_2 = -\sin\left(\frac{1}{2}s\right) \\ & \mathbf{m}_3 = \frac{1}{2} \gamma \end{array} \quad (63)$$

$$\begin{array}{ll} \text{Quaternions:} & \mathbf{q}_0 = \frac{1}{2} \sqrt{1 + \cos\left(\frac{1}{2}s\right)} \sqrt{1 + \cos(s)} \\ & \mathbf{q}_1 = \frac{1}{2} \tan\left(\frac{1}{2}s\right) \sqrt{1 + \cos\left(\frac{1}{2}s\right)} \sqrt{1 + \cos(s)} \\ & \mathbf{q}_2 = \frac{1}{2} \left(1 - \sec\left(\frac{1}{2}s\right)\right) \sqrt{1 + \cos\left(\frac{1}{2}s\right)} \sqrt{1 + \cos(s)} \\ & \mathbf{q}_3 = \frac{1}{2} \sqrt{\frac{1 + \cos(s)}{1 + \cos\left(\frac{1}{2}s\right)}} \sin\left(\frac{1}{2}s\right) \end{array} \quad (64)$$

We define the solution vector $\mathbf{U} := (\bar{\mathbf{r}}, \mathbf{n}, \mathbf{m}, \mathbf{q})$, the norm of which we use to plot the continuation path in Figure 2 for increasing λ .

3.4 Full Rod Construction

Once we obtain a numerical solution for (39)-(43), (44)-(47), (49)-(52), (57)-(59) on $[0, \pi]$, we construct the rest of the closed-loop on $[\pi, 2\pi]$ via a flip rotation by 180 degrees about

the \mathbf{e}_2 -axis. The following procedure is rigorously detailed in [8]. Denote the calculated solution to (39)-(42) for $s \in [0, \pi]$ by a superscript “c”, e.g. $\mathbf{r}^c(s)$ for the calculated rod centerline position. We represent the flip by the operator

$$\mathbf{E} = -(\mathbf{e}_1 \otimes \mathbf{e}_1) + (\mathbf{e}_2 \otimes \mathbf{e}_2) - (\mathbf{e}_3 \otimes \mathbf{e}_3). \quad (65)$$

The position of the centerline for $s \in [0, 2\pi]$ is given by

$$\mathbf{r}(s) = \begin{cases} \mathbf{r}^c(s) & s \in [0, \pi] \\ \mathbf{E}\mathbf{r}^c(2\pi - s) & s \in [\pi, 2\pi] \end{cases}. \quad (66)$$

The continuity of $\mathbf{r}(\cdot)$ at $s = \pi$ follows from (49), (50), and (65). It follows similarly that $\mathbf{r}(0) = \mathbf{r}(2\pi)$.

The extension of the rod’s orientation on $[\pi, 2\pi]$ is defined in terms of the director fields $\mathbf{d}_i(s)$:

$$\mathbf{d}_1(s) = \begin{cases} \mathbf{d}_1^c(s) & s \in [0, \pi] \\ \mathbf{E}\mathbf{d}_1^c(2\pi - s) & s \in [\pi, 2\pi] \end{cases}, \quad (67)$$

$$\mathbf{d}_2(s) = \begin{cases} \mathbf{d}_2^c(s) & s \in [0, \pi] \\ -\mathbf{E}\mathbf{d}_2^c(2\pi - s) & s \in [\pi, 2\pi] \end{cases}, \quad (68)$$

$$\mathbf{d}_3(s) = \begin{cases} \mathbf{d}_3^c(s) & s \in [0, \pi] \\ -\mathbf{E}\mathbf{d}_3^c(2\pi - s) & s \in [\pi, 2\pi] \end{cases}. \quad (69)$$

Observe that $\mathbf{d}_i(\cdot)$, $i = 1, 2, 3$ is continuous on $[0, 2\pi]$.

While the rod position and orientation are enough to reproduce the equilibrium configuration for the closed loop, we also give the extensions of the contact force and contact couple fields, \mathbf{n} and \mathbf{m} respectively, mainly for use in the stability analysis performed in Section 5. Following the results in [8], the required extensions are given by:

$$\mathbf{n}(s) = \begin{cases} \mathbf{n}^c(s) & s \in [0, \pi] \\ -\mathbf{E}\mathbf{n}^c(2\pi - s) & s \in [\pi, 2\pi] \end{cases}, \quad (70)$$

$$\mathbf{m}(s) = \begin{cases} \mathbf{m}^c(s) & s \in [0, \pi] \\ -\mathbf{E}\mathbf{m}^c(2\pi - s) & s \in [\pi, 2\pi] \end{cases}. \quad (71)$$

In view of (51)-(52), we see that $\mathbf{n}(\cdot)$ and $\mathbf{m}(\cdot)$ are each continuous at $s = \pi$. We further claim that $\mathbf{n}(0) = \mathbf{n}(2\pi)$ and $\mathbf{m}(0) = \mathbf{m}(2\pi)$. To see this, note that the global balance of forces and moments for the half rod on $[0, \pi]$, together with (51)-(52) reveal that $\mathbf{n}(0) \cdot \mathbf{e}_2 = \mathbf{m}(0) \cdot \mathbf{e}_2 = 0$. The claim now follows directly from (70)-(71).

4 Continuation

4.1 Numerical Implementation

AUTO-07P continuation and bifurcation software is employed to solve the system (39)-(42), subject to boundary conditions (44)-(47), (49)-(52), and (57)-(59) via collocation methods. Unless otherwise noted, the rod is divided into 30 mesh intervals with 4 collocation points

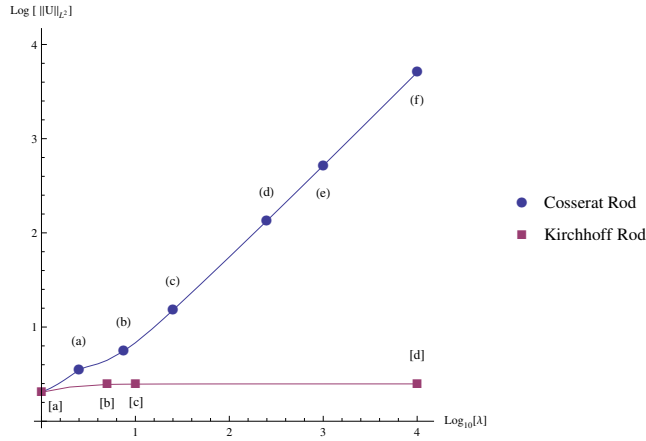


Fig. 2 L^2 norm of the solution vector \mathbf{U} versus λ for the Cosserat and Kirchhoff rod models on a Log-Log scale. We only plot the Cosserat rod where $c = 1.5$; other values of c produce qualitatively similar continuation paths. Labels along the continuation path in brackets and parenthesis refer to configurations shown in Figures 4 and 5 respectively.

per interval for a total of 121 nodes along the interval $[0, \pi]$. AUTO uses adaptive meshing set to update the mesh after every three continuation steps. The Newton solver is set to convergence tolerance of 10^{-7} . The step size for the parameter λ is initialized at 10^{-2} , but is adapted by AUTO as part of the pseudo-arclength method during calculations. More information on AUTO and numerical continuation is found in [5] and [6].

The centerline and orientation vectors from the solution in AUTO are graphed with Mathematica. The rod body is visualized in the \mathbf{d}_1 direction by a set scale value, ℓ , and the \mathbf{d}_2 direction by the distance $\frac{\ell}{\sqrt{\lambda}}$ to produce a visual three dimensional model. As the continuation is carried out, the rod cross-section is represented as becoming thinner (rather than wider) for graphical clarity.

4.2 Kirchhoff Rod Theory Results

Here we interpret the elastic moduli in (21)-(22) according to (19)-(20) yielding

$$\lambda = \frac{I_2}{I_1}, \quad (72)$$

$$\gamma = \frac{GJ}{EI_1}. \quad (73)$$

For an isotropic elastic rod with rectangular cross section (base b , thickness h , and $b \gg h$) the parameter λ is given by

$$\lambda = \frac{I_2}{I_1} = \left(\frac{b}{h}\right)^2. \quad (74)$$

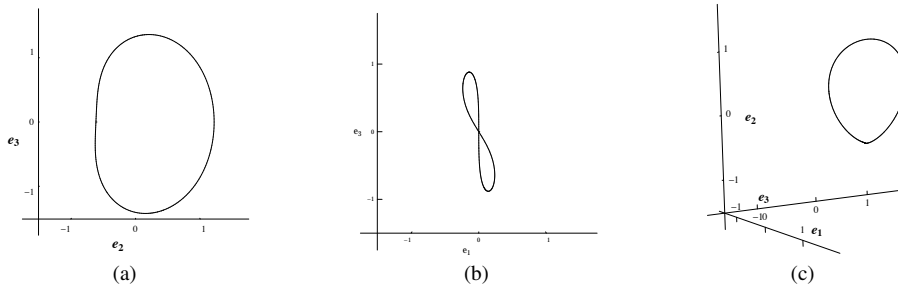


Fig. 3 Perspective views of the Kirchhoff rod's centerline after numerical continuation to $\lambda = 10^4$.

Formulas from strength of materials (cf. [2]) give

$$EI_1 = \frac{1}{12} E b h^3, \quad (75)$$

$$GJ = \frac{E}{2(1+\nu)} \left(\frac{1}{3} b h^3 \right), \quad (76)$$

where E is Young's modulus and ν is Poisson's ratio. Substituting this into (73) yields

$$\gamma = \frac{2}{1+\nu}. \quad (77)$$

We set $\nu = 1/3$ which corresponds to $\gamma = 3/2$. We pause to note here that different γ values in the allowed range did not produce qualitatively different equilibrium configurations in the numerical results.

Figures 3 and 4 depict some of the configurations obtained. These are in qualitative agreement with the smoothly varying configurations found in [13]. In particular, no solutions with localized twisting or bending were found.

4.3 Cosserat Rod Results

We use the constitutive relations in (21)-(23) and (32) for the Cosserat rod implementation. We examine three regimes: $c > 1$, $c = 1$, and $c < 1$. We start with $c > 1$ (specifically $c = 1.5$). Figures 5 and 6 depict a configuration with localized bending and twisting for $\lambda = 10^4$ in qualitative agreement with the configurations seen from the developable surface model in [16]. In addition, the curvature graphs in Figure 7 suggest that κ_3 is minimized in such configurations.

Figure 8 illustrates the distinct differences between the Cosserat models with $c < 1$, $c = 1$, and $c > 1$. For $c < 1$, the strip collapses inwards until self-contact occurs, while the $c = 1$ strip appears to get "stuck" between the two behaviors ($c < 1$ and $c > 1$) for large λ . We note further that in this case ($c = 1$), the convergence of the numerical continuation scheme becomes rather sluggish in comparison to the other two cases.

To quantitatively measure the effects of different values of c , we define the values

$$\|\kappa_i\| = \left(\int_0^\pi \kappa_i(s)^2 ds \right)^{1/2}. \quad (78)$$

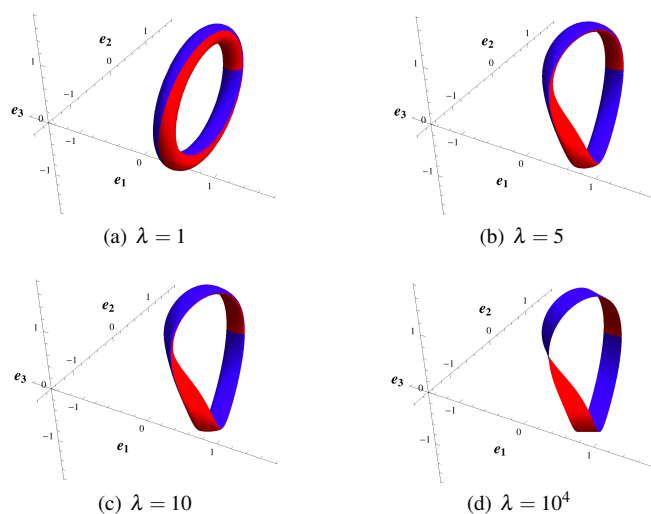


Fig. 4 Kirchhoff rod theory results. All plots have $\gamma = 1.5$ and $\mu = 0$. Note that the origin of the axes is at the point $(-1.5, -1.5, 0)$. Coloring is used to indicate the orientation of the strip.

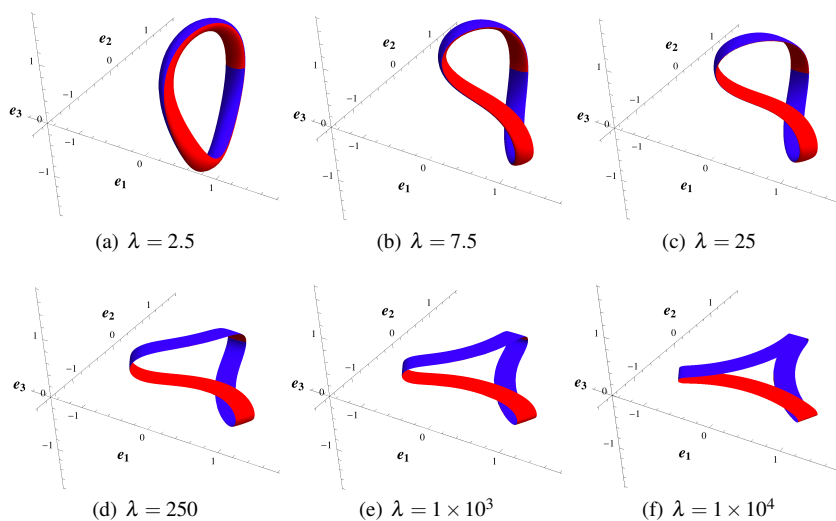


Fig. 5 Cosserat rod theory results. All pictures have $c = 1.5$ and $\mu = 0$. The starting $\lambda = 1$ configuration is omitted since it is identical to the configuration in Figure 4(a). Note that the origin of the axes is at the point $(-1.5, -1.5, 0)$.

From Figure 9, we observe that $\|\kappa_3\|$ approaches zero for $c > 1$ while $\|\kappa_2\|$ approaches zero for $c < 1$ as λ becomes large. Furthermore, Figure 9a shows that choosing smaller values of $c < 1$ causes $\|\kappa_2\|$ to asymptotically approach zero more quickly. Likewise, Figure 9b shows that larger magnitudes of $c > 1$ cause $\|\kappa_2\|$ to asymptotically approach zero more quickly as well.

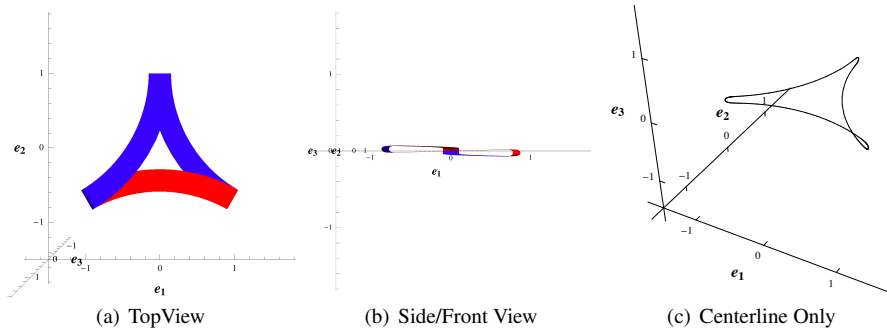


Fig. 6 Perspective views of the Cosserat rod theory results at $\lambda = 10^4$ and $c = 1.5$.

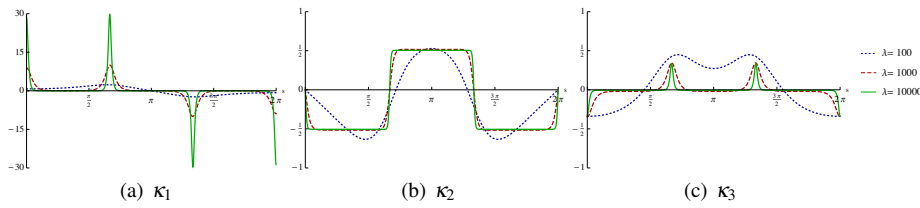


Fig. 7 Curvature plots for the Cosserat rod model with $c = 1.5$. Note that the scale for the plot of κ_1 is significantly different from the scale in plots of κ_2 and κ_3 .

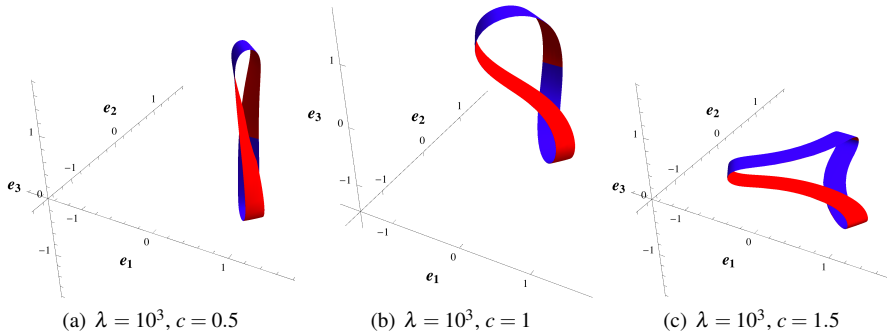


Fig. 8 Comparison of continuation results for Cosserat rods with different c values.

In addition, we can use $\|\kappa_3\|$ for a mesh convergence calculation. Calculations performed using 20, 30, and 40 mesh points on the rod for $c = 1.5$ did not produce significantly different values of $\|\kappa_3\|$ (figures and data presented to this point have been using 30 mesh points). Changing from 20 to 40 mesh points only changed the value of $\|\kappa_3\|$ by less than 0.01%.

Similar to results in [16], the equilibrium configuration for $c > 1$, λ large, appears to be an equilateral triangle. We quantitatively test that claim on the $c > 1$ configurations here for large λ . Using the points $\{s_1, s_2, s_3\}$ at each corner of the triangle and the standard euclidian

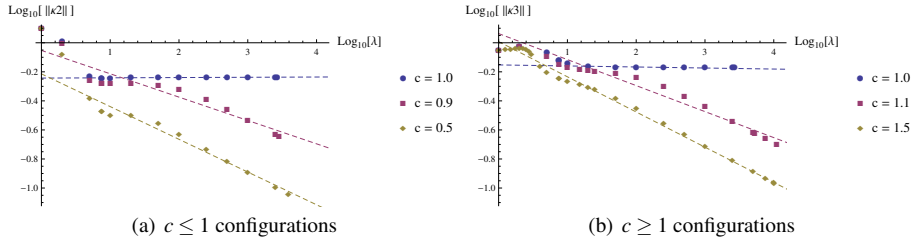


Fig. 9 $\text{Log}_{10} - \text{Log}_{10}$ plot of $\|\kappa_i\|$ versus the parameter λ for $i = 2, 3$ on the left and right respectively. Dotted lines represent least squares fit for points for $\lambda \geq 10$. This demonstrates how closely each Cosserat rod is to satisfying constraint (29) for rods with $c < 1$ or constraint (27) for rods with $c > 1$.

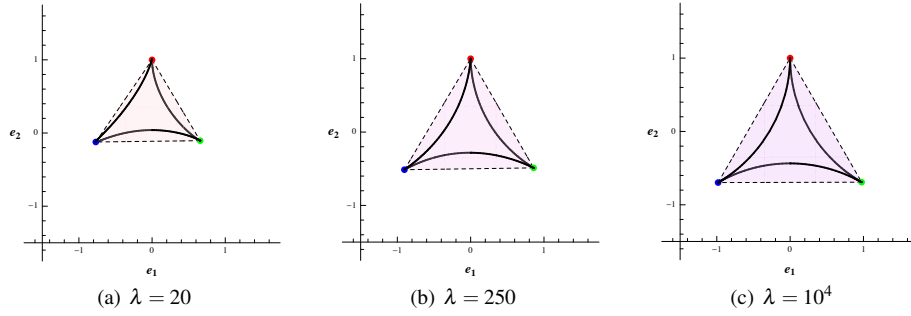


Fig. 10 Top views of the centerline with inscribed triangle and vertices indicated for $c = 1.5$. As λ becomes larger, the triangle becomes well defined and approaches an equilateral triangle.

metric $d[\cdot, \cdot]$, we define the values

$$\bar{S} = \text{average}(d[s_1, s_2], d[s_2, s_3], d[s_3, s_1]), \quad (79)$$

$$\delta_{ijk} = |d[s_i, s_j] - d[s_j, s_k]|, \quad (80)$$

where \bar{S} represent the average length of a side for the triangle, while δ_{ijk} is the difference in length between line segment ij and line segment jk . For an equilateral triangle, $\delta_{ijk} = 0$ for all i, j, k . Adding up all the combinations of δ_{ijk} measures how unequal the side lengths are and defines the quantity

$$\Delta S = \frac{1}{\bar{S}} (\delta_{123} + \delta_{231} + \delta_{321}), \quad (81)$$

where division by \bar{S} is used to get a percentage error independent of total triangle size. $\Delta S = 0$ indicates a perfect equilateral triangle. For $\lambda = 10^4$ we have $\Delta S = 2.13 \times 10^{-3}$ indicating the configuration is extremely close to an equilateral triangle. In addition, using a least-squares fit we find in Figure 11 that ΔS scales closely with λ^{-1} .

5 Stability

We determine the local stability of configurations found in sections 4.2 and 4.3 via linearized dynamic analysis about the equilibrium configurations, as developed in [12]. We consider

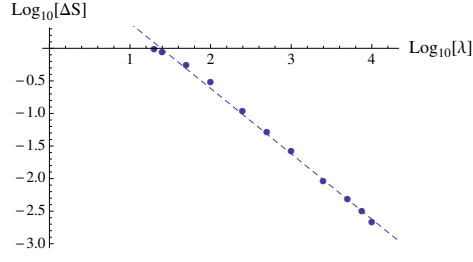


Fig. 11 $\text{Log}_{10} - \text{Log}_{10}$ plot of ΔS versus parameter λ . Only points with $\lambda \geq 20$ are plotted. These points are used in a least square fit to obtain the relationship $\Delta S = 24.6 \lambda^{-1.003}$ indicated by the dotted line. Final value at $\lambda = 10^4$ is $\Delta S = 2.13 \times 10^{-3}$.

the stability of the entire closed rod configuration on $[0, 2\pi]$ with respect to small perturbations. We first summarize the procedure of [12] in the context of our problem.

An unshearable-inextensible rod free from body forces or body couples is governed by,

$$\mathbf{n}' = \rho A \ddot{\mathbf{r}}, \quad (82)$$

$$\mathbf{m}' + \mathbf{r}' \times \mathbf{n} = \rho (\dot{\mathbf{I}} \mathbf{w}), \quad (83)$$

$$\mathbf{r}' \cdot \mathbf{R} \mathbf{e}_\alpha = 0, \quad \alpha = 1, 2 \quad (84)$$

$$\mathbf{r}' \cdot \mathbf{R} \mathbf{e}_3 = 1, \quad (85)$$

where ρ is the density of the rod, A is the cross-sectional area, \mathbf{I} is the moment of area tensor, \mathbf{w} is the angular velocity of the cross-sections, and the over dot $\dot{}$ indicates a derivative with respect to time. In particular, (82) and (83) correspond to balance of linear and angular momentum respectively. We multiply equations (82)-(85) by smooth fields η, ψ, ξ and integrate along the length of the rod yielding the weak form equation

$$G = \int_0^{2\pi} \left[(\rho A \ddot{\mathbf{r}} - \mathbf{n}') \cdot \eta + (\rho (\dot{\mathbf{I}} \mathbf{w}) - \mathbf{m}' - \mathbf{r}' \times \mathbf{n}) \cdot \psi + \xi_\alpha \mathbf{r}' \cdot \mathbf{R} \mathbf{e}_\alpha + \xi_3 (\mathbf{r}' \cdot \mathbf{R} \mathbf{e}_3 - 1) \right] ds, \quad (86)$$

where η, ψ , and ξ correspond to smooth variations in \mathbf{r}, \mathbf{R} , and \mathbf{n} respectively. After integrating by parts, G decomposes into the static and dynamic contributions

$$G_{dynamic} = \int_0^{2\pi} \left[\rho A \ddot{\mathbf{r}} \cdot \eta + \rho (\dot{\mathbf{I}} \mathbf{w}) \cdot \psi \right] ds, \quad (87)$$

$$G_{static} = \int_0^{2\pi} \left[\mathbf{n} \cdot (\eta' - \psi \times \mathbf{r}') + \mathbf{m} \cdot \psi' + \xi_\alpha \mathbf{r}' \cdot \mathbf{R} \mathbf{e}_\alpha + \xi_3 (\mathbf{r}' \cdot \mathbf{R} \mathbf{e}_3 - 1) \right] ds + [\mathbf{n} \cdot \eta + \mathbf{m} \cdot \psi]_0^1. \quad (88)$$

Since the contact couple, \mathbf{m} , is constitutively determined, we have

$$G(\mathbf{r}, \mathbf{R}, \mathbf{n}; \eta, \psi, \xi) = 0, \quad (89)$$

at a static equilibrium point. We now consider perturbations (denoted with subscript ε)

$$\mathbf{r}_\varepsilon = \mathbf{r} + \varepsilon \Delta \mathbf{r}, \quad (90)$$

$$\mathbf{R}_\varepsilon = \exp(\varepsilon \Delta \Theta) \mathbf{R}, \quad (91)$$

$$\mathbf{n}_\varepsilon = \mathbf{n} + \varepsilon \Delta \mathbf{n}, \quad (92)$$

where $\Delta \mathbf{r}$, $\Delta \mathbf{n}$, $\Delta \Theta$ are smooth admissible variations, $\exp(\cdot)$ denotes the matrix exponential, and $\Delta \Theta$ is a smooth admissible skew-symmetric matrix. We define $\Delta \theta = \text{axial}(\Delta \Theta)$. In addition, we define the vector

$$\Delta \zeta_0 = \begin{pmatrix} [\Delta \mathbf{r}] \\ [\Delta \theta] \\ [\Delta \mathbf{n}] \end{pmatrix}, \quad (93)$$

and time dependent perturbations of the form

$$\Delta \zeta = \Delta \zeta_0 e^{\sigma t}. \quad (94)$$

Taylor's expansion about an equilibrium point generates

$$G(\mathbf{r}_\varepsilon, \mathbf{R}_\varepsilon, \mathbf{n}_\varepsilon) = \varepsilon DG(\mathbf{r}, \mathbf{R}, \mathbf{n}) \Delta \zeta + o(\varepsilon |\Delta \zeta|). \quad (95)$$

Substituting (94) into the linear part of (95), we obtain the generalized eigenvalue problem

$$DG_{static} \Delta \zeta_0 = -\sigma^2 DG_{dynamic} \Delta \zeta_0. \quad (96)$$

where $\mu := -\sigma^2$ is the eigenvalue. As discussed in [12], the structure of (96) is nonstandard, due to the presence of the linearized constraints, e.g. (84)-(85), on the left side, which are equated to zero on the right side. Moreover, for conservative problems, like the one at hand, the eigenvalues are necessarily real: A negative eigenvalue, $\mu < 0$, indicates instability, since $\sigma = \sqrt{-\mu}$ in (94) engenders exponential growth; a positive eigenvalue implies that σ is purely imaginary, showing that (94) is oscillatory. Accordingly, the solution is stable if all eigenvalues are positive.

To calculate the eigenvalues in (96), we employ the finite-element method, as implemented in [12, 15]. We approximate the smooth test functions (η, ψ, ξ) and spatial perturbations $(\Delta \mathbf{r}, \Delta \theta, \Delta \mathbf{n})$ with piecewise linear functions. Nodal values for the variables $(\mathbf{r}, \mathbf{R}, \mathbf{n}, \mathbf{m})$ on $[0, 2\pi]$ are obtained from the continuation results on $[0, \pi]$ and symmetry transformations in (66)-(70) on $[\pi, 2\pi]$.

For the closed loop, we clamp both the position and the orientation of the rod at $s = 0$ and $s = 2\pi$. Assuming the rod is divided into N elements with $N + 1$ nodes, the boundary conditions are

$$\Delta \mathbf{r}^{(0)} = 0, \quad (97)$$

$$\Delta \theta^{(0)} = 0, \quad (98)$$

$$\Delta \mathbf{r}^{(N+1)} = 0, \quad (99)$$

$$\Delta \theta^{(N+1)} = 0. \quad (100)$$

These ensure that the $s = 0$ and $s = 2\pi$ ends of the rod will remain smoothly connected under any perturbation. In addition, (97)-(100) eliminate the six neutrally stable rigid-body modes corresponding to uniform translation and rotation of the closed rod and also one additional neutral degeneracy associated with the axial motion of the strip acting through its own fixed configuration [7, 8]. For the initial isotropic configuration ($\lambda = 1$), there is one remaining zero eigenvalue, due to a one-parameter family of solutions corresponding to continuous precession of the centerline configuration accompanied by rolling of the cross sections in the opposite sense, c.f. [7, 8, 9]. This degeneracy disappears for $\lambda > 1$.

The finite element calculation discretization is made in consonance with the discrete solution from the AUTO continuation. This requires 240 elements of variable length leading to

a 2169×2169 global matrix, DG_{static} . As detailed in [12], we reduce DG_{static} via an orthogonal transformation, based on the point-wise constraints, resulting in a symmetric, projected stiffness matrix of dimension 711×711 . As noted in [12], in a conservative problem like the one at hand, it is enough to check the signs of the smallest eigenvalues of the stiffness matrix in order to determine stability. We do this using MatLab for each equilibrium configuration for both the Kirchhoff rod and the Cosserat rod. Doing so for our computed configurations in the range $1 \leq \lambda \leq 10^4$, we find that both the Kirchhoff rod equilibria and Cosserat rod equilibria for $c > 1$ are all locally stable.

6 Concluding Remarks

The calculations (26)-(29) reveal a deficiency in the strategy employed in [13], viz., (29) alone (approached asymptotically) is not enough to ensure near developability of the thin elastic strip; (27) as well as (29) are required. In the limit this leads to a developable mid-surface with instantaneous axis of bending always perpendicular to the tangent of the centerline. Given (26), this is the best that can be expected from the special Cosserat theory. Of course (25) is not exact, and we don't strictly enforce (27) and (29). Rather we approach them via continuation - in the same spirit as [13]. In this way we are able to capture a wide range of behaviors - including those uncovered in [16] - employing only the simplest rod theory. The developable-surface theory of [14], [18] and employed in [16] is exact but also more complicated. We remark further that exact developability per se is an idealized modeling assumption.

It is interesting that the rate of growth of the torsional-modulus ratio must be slightly greater than that of the bending-modulus ratio, viz., $c > 1$ in (31), in order to capture the flat, nearly triangular localization depicted in Figure 5. In hindsight the reason for this is apparent: Returning to (18), in view of (21), (22) and (32), we see that the total stored energy of the strip has the form

$$E = \frac{1}{2} \int_0^{2\pi} (\kappa_1^2 + \lambda \kappa_2^2 + c\lambda \kappa_3^2) ds, \quad (101)$$

where λ is very large. With $c > 1$ the local energy price for twist is slightly higher than that for κ_2 -bending. Accordingly the rod essentially twists only in highly concentrated jumps over very small lengths, accompanied by smooth, small κ_2 -bending in between. This further engenders highly concentrated κ_1 -bending, which accommodates the concentrated twist, cf. Figure 7. When $c < 1$ the opposite happens: κ_2 -bending occurs only in highly concentrated jumps over very short lengths, accompanied by smooth, small twist in between. This gives rise to an elongated shape, cf. Figure 8(a).

Models of actual Möbius bands suggest the uniqueness and stability of the flip-symmetric solution. Although we can say nothing about the former, our local stability results of Section 5 are the first of their kind. In particular, stability is not discussed in either [13] or [16].

Acknowledgements This work was supported in part by the National Science Foundation through grants DMS-1007830 and DMS-1312377, which is gratefully acknowledged. We thank Roberto Paroni for providing us with his personal notes on the derivation of the Sadowsky-Wunderlich model.

References

1. Antman, S.S.: Nonlinear Problems of Elasticity. Springer New York (2005)

2. Den Hartog, J.: *Advanced Strength of Materials*. McGraw-Hill Book Company, New York (1952)
3. Dias, M.A., Audoly, B.: “Wunderlich, meet Kirchhoff”: A general and unified description of elastic ribbons and thin rods. Submitted to *Journal of Elasticity*
4. Do Carmo, M.: *Differential Geometry of Curves and Surfaces*. Prentice-Hall, Inc., Englewood Cliffs, NJ (1976)
5. Doedel, E.J.: Lecture notes on numerical analysis of nonlinear equations. *Numerical Continuation Methods for Dynamical Systems* (2007)
6. Doedel, E.J., Oldeman, B.E.: AUTO-07p: Continuation and Bifurcation Software for Ordinary Differential Equations (2009)
7. Domokos, G.: A group-theoretic approach to the geometry of elastic rings. *Journal of Nonlinear Science* **5**(6), 453–478 (1995)
8. Domokos, G., Healey, T.J.: Hidden Symmetry of Global Solutions in Twisted Elastic Rings. *Journal of Nonlinear Science* **11**(1), 47–67 (2001)
9. Healey, T.: Large rotatory oscillations of transversely isotropic rods: Spatio-temporal symmetry-breaking bifurcation. *SIAM Journal on Applied Mathematics* **52**(4), 1120–1135 (1992)
10. Healey, T.J., Mehta, P.: Straightforward computation of spatial equilibria of geometrically exact cosserat rods. *International Journal of Bifurcation and Chaos* **15**(3), 949–965 (2005)
11. Hornung, P.: Euler-Lagrange equations for variational problems on space curves. *Physical Review E* **81**(6), 1–5 (2010). DOI 10.1103/PhysRevE.81.066603
12. Kumar, A., Healey, T.J.: A generalized computational approach to stability of static equilibria of nonlinearly elastic rods in the presence of constraints. *Computer Methods in Applied Mechanics and Engineering* **199**(25-28), 1805–1815 (2010)
13. Mahadevan, L., Keller, J.B.: The Shape of a Mobius Band. *Proceedings of the Royal Society A: Mathematical, Physical and Engineering Sciences* **440**(1908), 149–162 (1993)
14. Sadowsky, M.: Ein elementarer Beweis für die Existenz eines abwickelbaren Möbiusschen Bandes und Zurückführung des geometrischen Problems auf ein Variationsproblem. pp. 412–415 (1930)
15. Simo, J., Vu-Quoc, L.: A Three Dimensional Finite-Strain Rod Model. Part II: Computational Aspects. *Computer methods in applied mechanics and engineering* **58**, 79–115 (1986)
16. Starostin, E.L., van Der Heijden, G.H.M.: The shape of a Möbius strip. *Nature materials* **6**(8), 563–7 (2007)
17. Starostin, E.L., van Der Heijden, G.H.M.: Force and moment balance equations for geometric variational problems on curves. *Physical Review E* **79**(6), 1–5 (2009)
18. Wunderlich, W.: Über ein abwickelbares Möbiusband. *Monatshefte für Mathematik* **66**(3), 276–289 (1962)